# Ultra-High Resolution Wideband on-Chip Spectrometer

**Mehedi Hasan**
**Mohammad Rad**
**Gazi Mahamud Hasan**
**Peng Liu**
**Patrick Dumais**
**Eric Bernier**
**Trevor J. Hall**
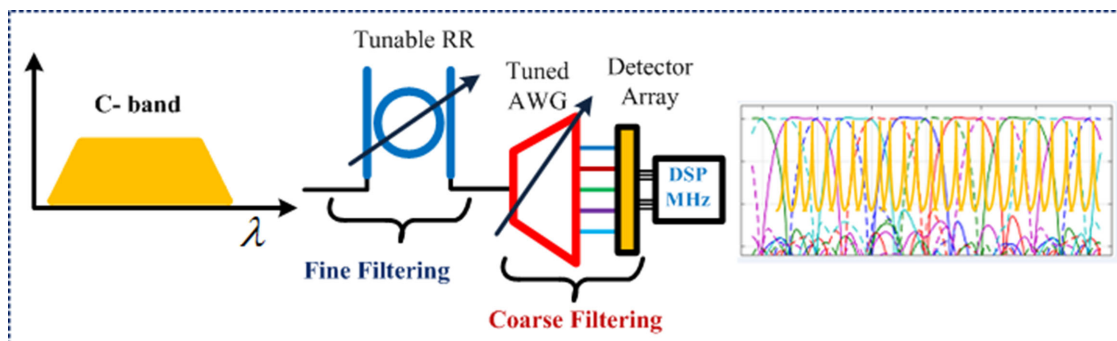
# Ultra-High Resolution Wideband on-Chip Spectrometer

**Mehedi Hasan** [ORCID],[1] **Mohammad Rad,**[2] **Gazi Mahamud Hasan,**[1] **Peng Liu,**[1] **Patrick Dumais** [ORCID],[2] **Eric Bernier,**[2] **and Trevor J. Hall** [ORCID][1]

[1]Photonic Technology Laboratory, Centre for Research in Photonics, Advanced Research Complex, University of Ottawa, Ottawa, ON K1N 6N5, Canada
[2]Huawei Technologies Canada, Kanata, ON K2K 3J1, Canada

**Abstract:** Monitoring the state of the optical network is a key enabler for programmability of network functions, protocols and efficient use of the spectrum. A particular challenge is to provide the SDN-EON controller with a panoramic view of the complete state of the optical spectrum. This paper describes an architecture for compact on-chip spectrometry targeting high resolution across the entire C-band to reliably and accurately measure the spectral profile of WDM signals in fixed and flex-grid architectures. An industry standard software tool is used to validate the performance of the spectrometer. The fabrication of the proposed design is found to be practical.

**Index Terms:** Spectrometer, ring resonator, mach-zehnder interferometer, arrayed waveguide grating, photonic integration, optical performance monitoring, optical transport networks.

## 1. Introduction

Software Defined Networking (SDN), Elastic Optical Networks (EON), and Artificial Intelligence (AI) have gained wide acceptance as they support network operators (Bell, Rogers, Verizon, etc.) in their quest to address the challenges of rapidly changing and demanding service requirements, while making efficient use of network resources [1], [2]. SDN allows programmability of network functions and protocols. EON allow the allocation of an arbitrary and appropriate spectral range and modulation format to an optical path according to application bandwidth and quality of service requirements taking into account optical physical layer attributes such as impairments [3]. AI allows the network to provision resources in response to current service requests while learning from the past to improve network efficiency and effectiveness [4].

SDNs scale by control and adaptive management, and handle changing demand and resources to achieve energy, resource efficiency and sustainability. Applying SDN principles to the physical layer that includes optical components, such as wavelength switches, fibre, add/drop mux/de-mux, amplifiers, filters, and sensors; requires fully programmable functions be they implemented in optics or electronics. As a consequence of the rigidity of the physical layer infrastructure, SDN research has focused principally on the higher digital electronic layers of the network. Applying SDN to the optical transport network could enhance both operational management in terms of cost saving and service layer performance such as fast connection turn-up, margin squeezing or health monitoring

of the network. The adaptability provided from AI combined with the flexibility of SDN & EON along with the extremely fast processing capability of optical devices will transform the existing transport networks into a next-generation SDN-enabled energy efficient optical transport network.

Optical performance monitoring (OPM) is critical to this vision as it is necessary that the SDN-EON-AI controller is provided with sufficient and accurate knowledge of the state of the network to fulfill its function. Network management agents or optimization algorithms require up to date telemetry data of the network on links, components and operating points of service (WDM traffic channels in the case of transport optics). Monitoring information can be used for better resource optimization to maximize the reach versus rate. OPM information can also be used for performance prediction and planning in case of network reconfiguration, capacity scaling or network or component fault recovery. The monitoring information includes power, loss, bit-error-rate (BER), optical signal-to-noise-ratio (OSNR), electrical signal-to-noise ratio (ESNR), etc. In practice any parameter measured in the network can be used for the purpose of OPM. However, power is a strong indication of performance in optical systems as like other systems and hence OPM is used to refer to "power" in this manuscript.

Power measurement (monitoring) or spectrum sensing, while seemingly very simple and basic, is still challenging in transport optics especially in WDM networks. Typically, WDM channels are spread from 1530 nm to 1570 nm, i.e., across around 40 nm of fiber optic bandwidth. Traditional WDM channels are spaced at known and fixed locations of the WDM spectrum (50 GHz or 100 GHz ITU spectrum). However, current elastic optical networks are following more and more flex-grid channel profiles where the channel center wavelength can be at any place in the spectrum with much finer resolutions (e.g. smaller than 6.25 GHz) and they also can have different power profiles (i.e., bandwidth and power spectral density). Power measurement is done by OPM cards traditionally where a tunable filter sweeps the spectrum (C band) typically with 50 GHz resolution and hence ITU channel power readings become available. OPM cards are large; consume considerable power; and, most important, are expensive. As a result, they are only available at few points in the network. Typically, reconfigurable add-drop modules (ROADMs) are equipped with OPM cards. Since existing power measurements are based on ITU, flex ready spectrum measurements are adopted for flex grid systems. New modules capable of performing power measurement for desired location (center wavelength) and desired resolution (known bandwidth) are being used in flex-grid ready ROADM architectures. However, they still suffer from the cost issue and hence spectrum measurement is only available at add-drop nodes. ROADMs with high degrees usually share an OPM module for the purpose of spectrum measurement. This makes the OPM speed slow depending on the number of lines it supports. Amplifier nodes do not have power reading capabilities. Therefore, almost all analysis of photonic layer optimizations uses analytical, semi-analytical, or machine learned based modeling to estimate the performance of WDM channels in a section (ROADM-to-ROADM).

Reliable spectral measurement across the network is therefore a key enabling technology. Complete knowledge of the state of the network is a prerequisite to enabling SDN-EON-AI to make effective use of colour-, direction-, contention-, grid-less, filter-, gap-less ROADM, flexible channels centre frequencies and width, flexible sub-carriers in super-channels, flexible modulation formats and forward error control coding transponders, and impairment-aware wavelength routing and spectral assignment. The absence of OPM (with focus on power measurement) makes it very difficult to have reliable performance estimation or have the models trained and fed with proper live and accurate measurement across the network for the purpose of performance optimizations. Knowledge of spectral content in a section of optical networks is of great value for operators and photonics infra-structure owners.

A large variety of on-chip spectrometer designs have been unveiled and realized over the past decade such as cascaded ring resonator (RR) arrayed waveguide grating (AWG) architecture [5]–[6], dispersive configurations (arrayed waveguide gratings (AWG) [7], echelle gratings (EG) [7] or cascaded micro-ring resonators [8], cascaded Mach-Zehnder interferometer (MZI) based processor [9]; and discrete Fourier transform infrared spectroscopy [10]. In [5] the authors propose a combined architecture where the ring and AWGs need to be tuned to match the ring response

with the AWG center wavelength. Depending on the number of channels, fixed grid reading of the spectrum is achieved. Similar to the previous prior art the authors of [6] proposed a cascaded architecture where a ring resonator (RR) is followed by a parallel pair of arrayed waveguide gratings (AWG) with different center wavelengths to reduce the cross talk. The center wavelength of the AWGs must differ by half a channel spacing for proper operation but there is no mention of if and how the whole spectrum may be scanned. When the RR is not tuned to an AWG channel passband center, the spectrometer will suffer increased insertion loss and channel leakage (cross talk) with increased detuning. In addition to that, EG and AWGs have been proposed by Xiang *et al.* [8] to construct spectrometers capable of operation over a broad range of different wavelength. The resolution is restricted by the number of samples of the spectrum by the fixed number of EG/AWG channels. A multiple ring resonator in cascade architecture has been proposed in [8] for high resolution spectrum measurement. These architectures have proven to be extremely complicated to control and calibrate in a reliable fashion due to the fact that two or more very sensitive components (RR) are needed to be tuned together. On the other hand, in [9] a fast-Fourier transformation (FFT)-like approach is used by performing multiple measurements of the filtered spectrum. The authors demonstrate a resolution of 23 pm ($\sim$2.9 GHz) over a 184 pm range about 1550 nm. Sub-GHz resolution seems to be within reach but entire C band coverage remains challenging as it requires multiple arms (up to 10) which imposes significant loss, complex control and measurement dynamics. Following a similar approach, Kita *et al.* [10] proposed a new signal processing technique performed electro-optically where a combination of numerous measurements with data processing provides the desired high-resolution power measurement across a desired band. To achieve sub-GHz resolution more than 10 stages are needed. Therefore, this strategy and architecture suffers similarly in scaling when high resolution spectrum sensing over a wide band is needed. In summary, the existing measurement technologies fail to combine acceptable resolutions with wideband operation and do not support feasible integration with other products which limits their deployment mainly due to high cost, loss and foot print. In addition, the requirement of sub-GHz resolution bandwidth to reliably and accurately distinguish the individual carriers in a densely packed multi-carrier super-channels or to monitor the differential power of adjacent channels in fixed and flex-grid architectures with a large free-spectral range for transparent operation across the entire C band 1530 nm-1565 nm for an integrated solution remains challenging.

In this paper, the design of a technologically viable compact on-chip high-resolution wideband spectrometer is presented and verified by software simulation using an industry standard tool. A novel and original approach to coordinated tuning of the individual stages enables the spectrometer to scan the entire C-band with better than 1 GHz resolution using only three stages and two controls. The target application is to measure the spectral profile of WDM signals accurately in flex- and fixed- grid architectures across the entire C-band 1530 nm-1565 nm with minimum scan time and better than 1 GHz frequency accuracy. The photonic integration of the circuit architecture can be implemented using a mature fabrication technology; low index contrast Silica on Silica or CMOS compatible low loss $Si_3N_4$ photonic integration platform. However, to meet the technical specifications such as compact size and high-resolution bandwidth, the $Si_3N_4$ platform is preferred due to its impressive agreement between simulation and practical measurement for the components used in this design architecture [11]–[14].

## 2. Proposed Spectrometer Circuit Architecture

The circuit architecture of the proposed spectrometer [15] is illustrated schematically in Fig. 1. It consists of three stages. The first stage is a ring resonator (RR) which has the function of defining the spectrometer resolution. It provides a periodic train of resonances each with bandwidth <1 GHz and spaced by its free-spectral range (FSR). It is tuneable in frequency over one FSR. The final stage is an arrayed waveguide grating (AWG) which has the function of isolating one RR resonance in each output channel. Each channel has a −3 dB passband width equal to half the channel spacing. The output channel frequency spacing is equal to the FSR of the RR. The central stage has the function of ensuring to a good approximation that the centre frequency of each AWG output
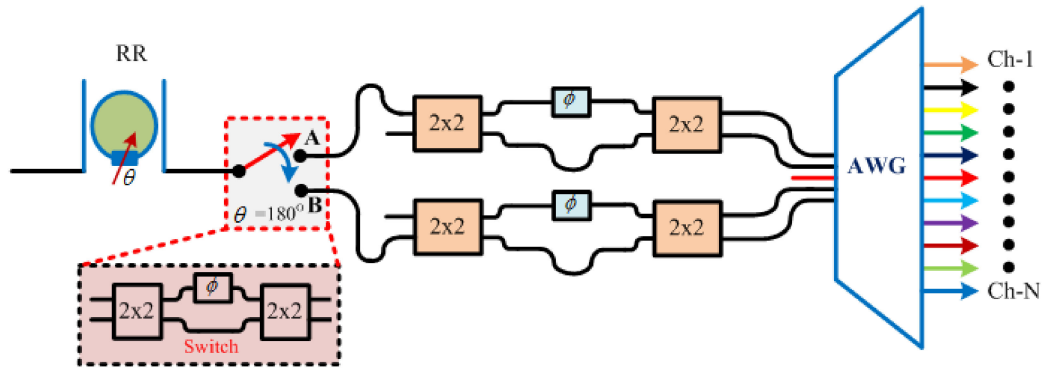
Fig. 1. Schematic of the proposed spectrometer. AWG, arrayed waveguide grating.
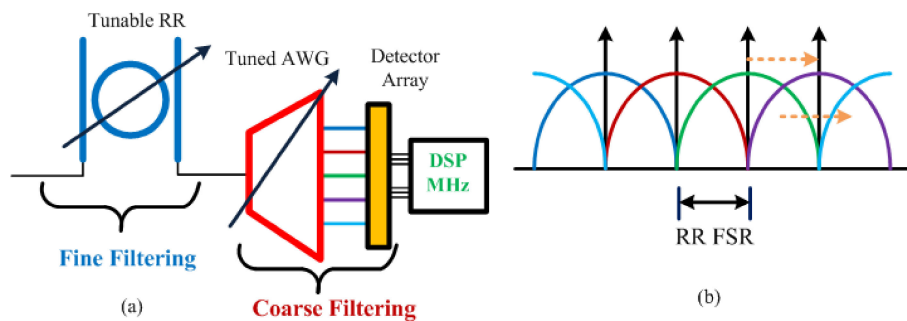


Fig. 2. (a) Tunable RR & AWG; DAQ, data acquisition; (b) Tracking of RR comb (grey arrows) & AWG channels (peaked curves).

channel passband tracks the centre frequency of their associated RR resonance. It consists of a parallel mirrored pair of nominally identical Mach-Zehnder delay interferometers (MZDI) with FSR equal to the AWG channel spacing and hence to the FSR of the RR. The construction of the MZDI can be made either by using 2 × 2 directional couplers or multimode interference (MMI) couplers. The four outputs of the central stage are connected via equal optical path length waveguides to four of five adjacent AWG input channels omitting the centre channel. The AWG input channel frequency spacing is equal to half the AWG output channel spacing. The Mach-Zehnder interferometer (MZI) that precedes the MZDI pair is used as a switch that selects the active MZDI and hence the active pair of AWG input channels of the four equipped AWG input channels.

The spectrometer has two controls: a first control to tune the RR and a second to toggle the MZI switch. A phase change of $\Delta\theta \in [0, 2\pi]$ within the RR provided by a phase shift element is used to scan cyclically the RR resonant frequency comb over one FSR. There are two phases within this operating cycle that correspond to the state of the switch. The switch toggles at the mid-point and the end point of the scan as determined by the first control. These two controls are the only dynamic controls needed. However, it is prudent to equip the MZDI stages with quasi-static (pre-set) phase trimmers to compensate any phase bias errors due to fabrication process variations. There is some freedom of choice in the selection of the FSR and hence the total number of AWG output channels required to operate over the entire C-band. Reported experimental demonstrations of the components, our device and circuit simulations, and the process development kit support the practicality of the demonstration of a spectrometer that meets the following specifications.

To isolate an individual RR resonance within an AWG channel, ideally the comb of AWG passband centre frequencies tracks the comb of RR resonant frequencies as the spectrometer is scanned, as illustrated schematically in Fig. 2 (a, b). The benefits of ganged tuning are:

minimisation of excess loss; tuning invariant channel transmission; and, an AWG adjacent channel crosstalk that is the best value (passband centre) rather than the worst value (passband edges). During the two phases of the scan, a data acquisition system (DAQ) acquires samples of the optical power monitored by photodetectors placed at the AWG outputs. Post processing of the acquired data may be further optimized for an increased effective measurement resolution. In principle, the AWG output channel spectra may be translated in frequency by translating the input waveguide across the input aperture of its first star coupler. An optical phased array (OPA) can be used to perform the translation of the input field profile. A necessary condition is that translation per unit frequency change of the OPA output equals that of the AWG input. The OPA may be based on a secondary AWG having an FSR equal to the primary AWG output channel frequency spacing. The secondary AWG output star coupler and the primary AWG input star coupler may be merged. However, the defocus caused by opposite sign curvature of the secondary AWG image field and the principal AWG object field strictly should be compensated by a field lens within the merged couplers. An alternative more practical approach adopted in this work is to accept a discrete approximation to the translation of the input field profile and connect the two-star couplers by N waveguides of the same optical path length. In the discrete case the output channel frequency spacing of the OPA should equal the input channel frequency spacing of the primary AWG and the OPA may be implemented by a dimension N generalised Mach-Zehnder Interferometer (GMZI) rather than by a secondary AWG.

A more serious problem follows from field being split between the two extrema of the beam steering aperture at the frequency at which the field profile should fly-back. Over the fly back transition in the transmission this result, in two adjacent RR resonances being passed via the same output port giving rise to unacceptable crosstalk at the edges of the tuning range. The remedy is to use two OPA-AWG units offset in frequency and to select the unit offering low crosstalk at a particular tuning. With this expedient it is sufficient to use a Mach-Zehnder interferometer (MZI) as a dimension N = 2 discrete approximation to an OPA.

Consider an MZI–AWG with input channel frequency spacing and output channel bandwidth equal to one half of its output channel frequency spacing $\Delta\omega$. A 2 × 2 MZI has an amplitude transmission matrix:

$$T_{MZI} = \begin{bmatrix} \sin(\varphi/2) & \cos(\varphi/2) \\ \cos(\varphi/2) & -\sin(\varphi/2) \end{bmatrix} \tag{1}$$

where $\varphi$ is the phase imbalance between its arms. It is easily verified that this transmission matrix satisfies energy conservation. Fig. 3 shows the basic amplitude transmission of an MZI, when light is launched from different input ports.

The period of the *amplitude* transmission matrix defined by Eq. 1 is 720 degrees. However, the phase imbalance of the arms leads to an $\exp(\varphi/2)$ scalar pre-multiplier neglected in Eq. 1 which ensures the overall MZI is invariant to a 360 degree change of $\varphi$. Accordingly, Fig 3(b) and (d) are only shown over a range of 360 degrees. Take the MZI port with $\cos(\varphi/2)$ dependence to be connected to the reference input channel of the AWG and the MZI port with $\sin(\varphi/2)$ dependence to be connected to the upshifted frequency input channel.

The amplitude transmission of a given output port is:

$$T_{AWG}(\omega) = H(\omega)\cos(\varphi/2) + H(\omega - \Delta\omega/2)\sin(\varphi/2) \tag{2}$$

where $H(\omega)$ is the transmission function of an AWG which may be taken as real to good accuracy and $\omega$ is the frequency offset from the centre of the passband. Now let us consider that $\varphi = \omega\tau$, where $\tau = 2\pi/\Delta\omega$, is the delay that must be applied in one of the arms of the MZI and $\Delta\omega$ is the AWG channel frequency spacing. The transmission at selected values of detuning is given by Table 2.

When $\omega\tau = 0$ ($\varphi = 0$), as per Fig. 3(b) the MATP port is active only, hence the amplitude transmission of the AWG is only $H(\omega)$. For $0° < \varphi < 180°$, the amplitude transmission of the MZI output ports have the same sign and there is constructive interference between the superimposed AWG amplitude transmissions. This corresponds to the desired frequency tracking behavior as
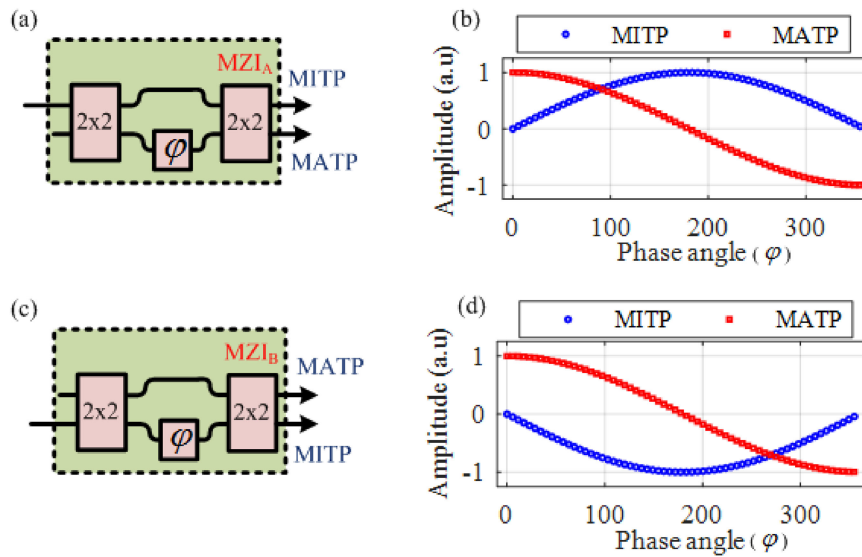
Fig. 3. Schematic of an MZI with input from upper port (a) and lower port: (c) and corresponding (b) & (d) amplitude transmission plot. MITP, minimum transmission point; MATP, maximum transmission point.

TABLE 1

Sub-System Design Specifications for the Proposed Spectrometer

| Design specifications | Comments | Remarks |
|---|---|---|
| RR free spectral range (GHz) | 50 | |
| MZI free spectral range (GHz) | 50 | Equal to the free spectral range of RR |
| AWG output channel spacing (GHz) | 50 | Equal to the free spectral range of RR |
| AWG output channel bandwidth (GHz) | 25 | Half of AWG output channel spacing |
| AWG input channel spacing (GHz) | 25 | Half of AWG output channel spacing |
| Number of AWG output channel | 88 | |
| Total spectrum covered (THz) | 4.4 | $88 \times 50 = 4400$ GHz (entire C band) |

TABLE 2

Transmission of the $MZI_A$-AWG Output Channel for $MZI_A$ Phase Bias Variation From $0°$ to $360°$

| AWG transmission | $\omega$ | | | | | | Remarks |
|---|---|---|---|---|---|---|---|
| | 0 | $\Delta\omega/4$ | $\Delta\omega/2$ | $-\Delta\omega/2$ | $-\Delta\omega/4$ | $\Delta\omega$ | The AWG tracks the RR resonant frequency correctly over the first half of the RR/MZI FSR only corresponding to $MZI_A$ bias $0°$ to $180°$ |
| $T_{AWG}(\omega)$ | 1 | 1 | 1 | -1 | 0 | 1 | |

summarised by Table 2. As the input channel frequency spacing of the AWG is set to 25 GHz, the MZI-AWG combination track over half of the output channel frequency spacing. When $180° < \varphi < 360°$, as shown in Fig. 3(b) the amplitude transmission of the MZI are opposite in sign resulting in destructive interference between the superimposed AWG amplitude transmissions. As a result, the remaining half the FSR is taken up by the undesired fly-back response.

The fly-back may be corrected using an alternative $MZI_B$-AWG arrangement with the MZI port with $\cos(\varphi/2)$ dependence connected to the reference input channel of the AWG and the MZI port with $-\sin(\varphi/2)$ connected to the upshifted frequency input channel. As shown in Fig. 3(d),

TABLE 3

Transmission of $\text{MZI}_B$-AWG Output Channel for $\text{MZI}_B$ Phase Bias Variation From $0°$ to $360°$.

| AWG transmission | $\omega$ | | | | | | Remarks |
|---|---|---|---|---|---|---|---|
| | 0 | $\Delta\omega/4$ | $\Delta\omega/2$ | $-\Delta\omega/2$ | $-\Delta\omega/4$ | $\Delta\omega$ | The AWG tracks the RR resonant frequency correctly over the second half the RR/MZI FSR only corresponding to $\text{MZI}_B$ bias 180° to 360° |
| $T_{AWG}(\omega)$ | 1 | 0 | -1 | 1 | 1 | 1 | |

the amplitude of the MZI output ports have the same sign and create constructive interference between the superimposed AWG amplitude transmission for $180° < \varphi < 360°$. The new form of the previously described amplitude transmission at the same output port becomes,

$$T_{AWG}\ (\omega) = \ H\ (\omega)\cos\ (\varphi/2) - H\ (\omega - \Delta\omega/2)\sin\ (\varphi/2) \tag{3}$$

The frequency tracking behavior of the $\text{MZI}_B$-AWG arrangement is summarised in the Table 3 and can be seen to be complementary to the frequency tracking behavior of the $\text{MZI}_A$-AWG arrangement summarised in Table 2: when $\text{MZI}_A$-AWG commences fly-back, $\text{MZI}_B$-AWG tracks correctly and vice versa.

Fig. 4(a-b) depicts the combination of the $\text{MZI}_A$-AWG and $\text{MZI}_B$-AWG with the simulated (i-x) frequency tracking behavior at different MZI phase bias. As found in the earlier analysis, the $\text{MZI}_A$-AWG combination tracks the RR resonance frequency correctly up to $\Delta\omega/2$ or 180° phase bias of the $\text{MZI}_A$, whereas $\text{MZI}_B$-AWG tracks the RR resonance frequency correctly from 180° to 360° phase bias. A phase bias ranging from 180° to 360° is equivalent to a phase bias ranging from 180° to 0°. Consequently, the circuit architectures track in opposite directions the same 0 GHz to 25 GHz span of the 50 GHz channel frequency spacing. To overcome this problem, the resolution during the fly-back phase $\text{MZI}_A$-AWG is to hand over to an alternative $\text{MZI}_B$-AWG with the MZI port with $\cos(\varphi/2)$ dependence connected to the reference input channel of the AWG and the MZI port with $-\sin(\varphi/2)$ dependence connected to the downshifted frequency input channel of the AWG. This arrangement advantageously eliminates the cross-over interconnection.

The amplitude transmission at the same output port is modified to:

$$T_{AWG}\ (\omega) = \ H\ (\omega)\cos\ (\varphi/2) - H\ (\omega + \Delta\omega/2)\sin\ (\varphi/2) \tag{4}$$

which during the fly-back phase of $\text{MZI}_A$ gives the desired frequency tracking over the $-25$ GHz to 0 GHz span of the 50 GHz channel frequency spacing:

$$T_{AWG}\ (\omega) = 1 \ \omega = -\Delta\omega/2$$
$$T_{AWG}\ (\omega) = 1 \ \omega = -\Delta\omega/4$$
$$T_{AWG}\ (\omega) = 1 \ \omega = 0 \tag{5}$$

Note that at $\omega = 0, \ \pm\Delta\omega/2$, where handover occurs the two MZI-AWG channel outputs agree. Consequently $\text{MZI}_A$-AWG and $\text{MZI}_B$-AWG combine with handover to successfully track the full span ($-25$ GHz to $+25$ GHz) of the channel frequency spacing (50 GHz). To economise on hardware, one would like to use a switch to select the MZI input port and rearrange the connection of its two outputs between a three input AWG as shown in Fig. 5. However, a switch to rearrange the MZI outputs could introduce phase errors. It is consequently preferable to use two nominally identical MZDI to drive two pairs of adjacent ports separated by an unequipped central input port of a 5-input port AWG as shown in Fig. 1. The handover is then between the set of output ports and the same set displaced by one port. The data acquisition system can resolve this shift trivially.

The simulated output channel spectra of the AWG for a wide range of frequencies is shown in Fig. 6. The spectra shown in Fig. 6 provide intuition that the spectrometer may be understood as an RR working into a pair of passband-flattened AWGs with interleaved output channel spectra.
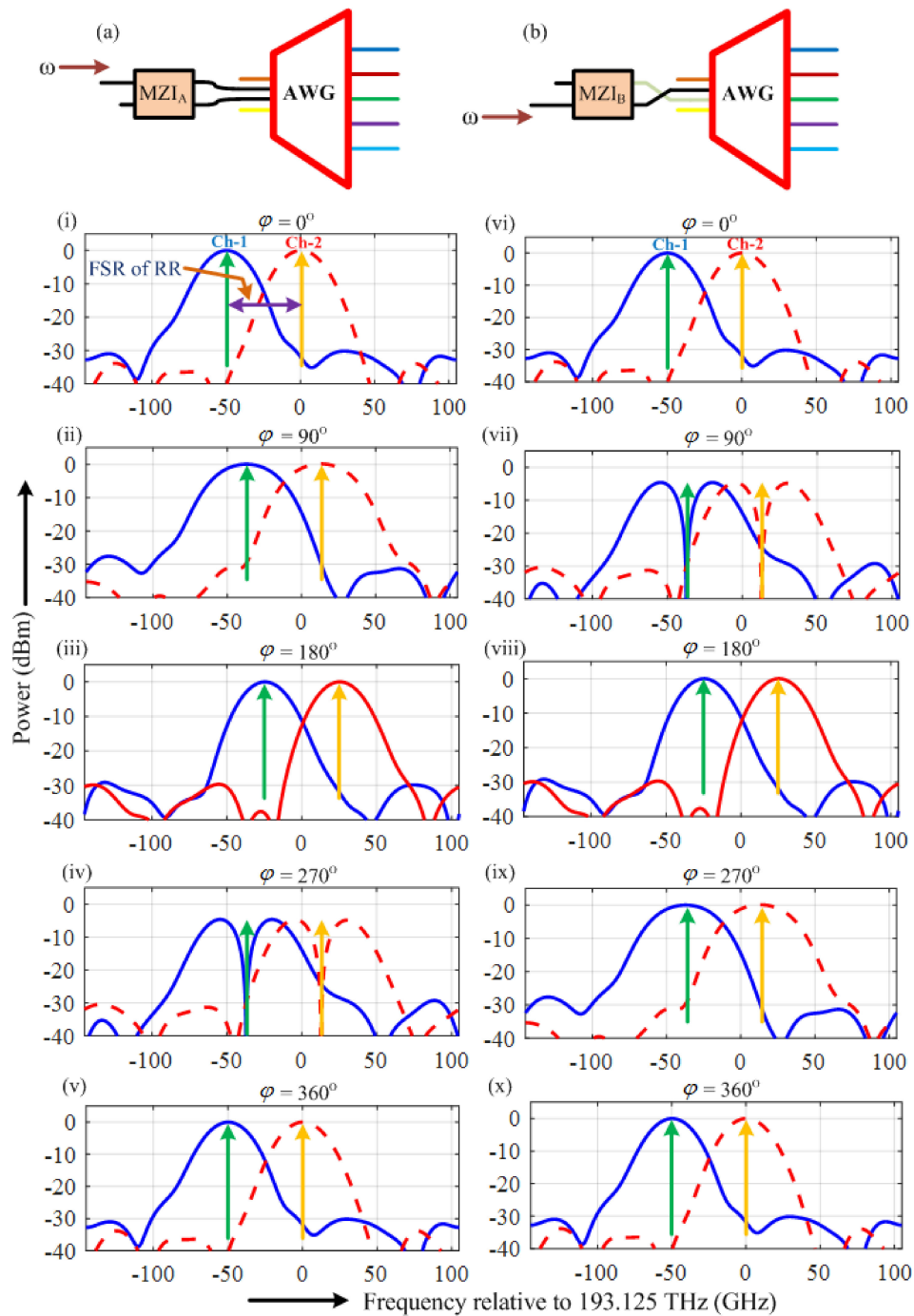
Fig. 4. MZI-AWG combination to correct the fly-back problem; (a) light is injected from the upper input port with corresponding amplitude transmission (i–v) of MZI$_A$-AWG combination at different phase bias; (b) light is injected from the lower input port with amplitude transmission(vi –x) of MZI$_B$-AWG combination at different phase bias of the MZI.
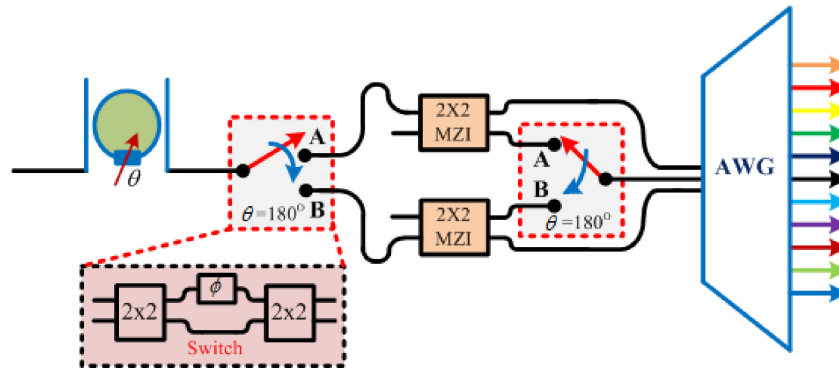
Fig. 5. Schematic diagram of the circuit architecture that can overcome the fly back problem and track the whole FSR of the RR.
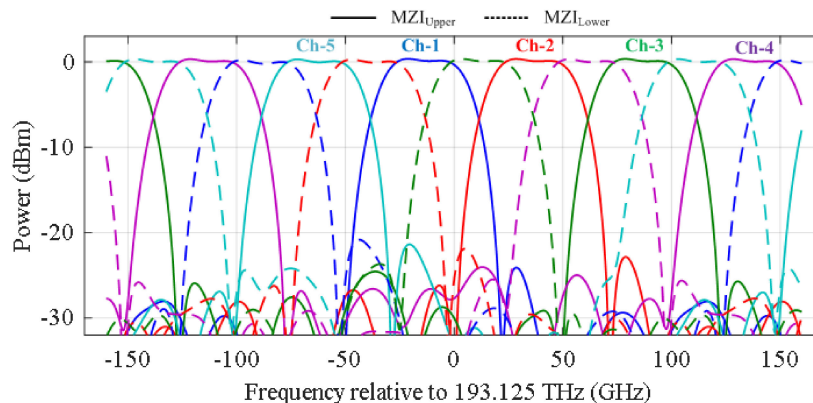


Fig. 6. AWG output channel spectra when both MZDI are auto-tuned by a delay line with an FSR equal to the AWG output channel frequency spacing. The channel spectra corresponding to the two different switch states are interleaved.

However, this does not imply that any approach to a passband flattening mechanism will suffice. The mechanism of choice is ganged tuning of the RR and AWG via (a good approximation to) translation of the input across the aperture of the first star coupler. This mechanism offers not only the best of low adjacent channel leakage found at the centre of channel passband rather than the worst of adjacent channel leakage found at the edges of the channel of the basic AWG but also it offers a means to merge the two interleaved AWGs into a single consolidated AWG which halves the number of output channels; the number of photodetectors; and the footprint size otherwise required.

## 3. Simulation Results

VPIphotonics software simulation is used to validate the theoretical prediction. Fig. 7. shows a schematic of the spectrometer stripped of the RR and with waveguide delay-lines and frequency independent static phase shift elements denoted by the symbol $\tau$. The phase shifts are adjusted manually to bias the upper and lower MZI stages and to switch between them. The switch is used to select the upper MZI (MZI$_A$) in the first phase illustrated in Fig. 4(i-v) and the lower MZI (MZI$_B$) in the second phase illustrated (Fig. 4(vi-x)). For better understanding the concept, a 5 channel AWG with an FSR of 250 GHz ($5 \times 50$ GHz) is used for simulation.
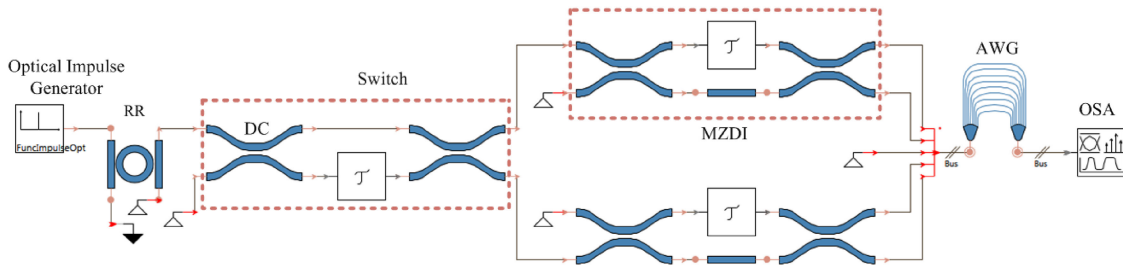
Fig. 7. VPI schematic of a circuit architecture for the purpose of demonstrating the operational principles by simulation; DC, directional coupler; OSA, optical spectrum analyzer.

To achieve auto-tuning the phase-shift elements presents in Fig. 4, are replaced by the delay lines. In this case (50 GHz output channel frequency spacing) the delay is chosen to set an FSR of 50 GHz. Fig. 8. shows the output of the AWG when both MZI are auto-tuned in this way. The flat passband and steep transitions between pass and reject bands are notable. The channel spectra corresponding to the two different switch states are interleaved. In the proposed architecture, only the RR will be tuned over one FSR for spectral sensing. One phase shifter for each MZI is included to align the MZI FSR with the AWG output channel spectra. It remains constant once the alignment (if required) is done.

Fig. 8. illustrates the output channel spectra over the full scanning cycle of the proposed spectrometer obtained by tuning the RR over one FSR. The switched MZDI-AWG succeeds in isolating one RR resonance with sub-GHz bandwidth within each AWG channel; the peak of the resonance is substantially constant as the ring resonance frequency is scanned across its 50 GHz FSR thereby providing a continuous spectrum across the whole operating band; and, the adjacent channel crosstalk is negligible. It may be observed that the selection of the upper MZI provides a flat response over half the channel frequency spacing corresponding to a phase bias of 0 to $-\pi$ radians and selection of the lower MZI provides a flat response over the remaining half of the channel frequency spacing corresponding to a phase bias of $-\pi$ to $-2\pi$ radians. Moreover, the readings of either selection agree at the two handover transitions in the scanning cycle one at a phase bias of 0, $-2\pi$ and one at a phase bias of $-\pi$. The contiguous flat response across the band is a noticeable feature.

## 4. Discussion

A combination of software simulation is used to study further the integration feasibility of the proposed architecture. VPIphotonics is used for the circuit simulation whereas, Photon Design along with MATLAB is used to verify the function of the individual components that comprise the architecture. The simplicity of the structure (3-stages) and control (2-controls) renders practical implementation as a single photonic integrated circuit. The proposed spectrometer can be fabricated in any mature fabrication platform. However, the resolution bandwidth of the spectrometer primarily depends on the insertion loss (dB/turn) of the RR. An integration platform supporting loss-loss waveguides and careful attention to the design of the RR couplers to minimise their excess loss are therefore paramount. Hence in order to meet the specification of the proposed spectrometer, the CMOS compatible $Si_3N_4$ photonic integration platform has been selected as it offers low loss, tight confinement, low dispersion and a mature thermo-optic phase shifter technology. There are ample reports in the literature of the technological verification of SSC, MMI, tunable RR, and sub-circuits such as MZ(D)I [11]–[13] and modest port count AWG fabricated using the $Si_3N_4$ integration platform [14].

For effective use of resources, the fabrication plan envisaged access to multi-project wafer MPW runs for test structures followed by a custom wafer run for fabrication of prototypes for
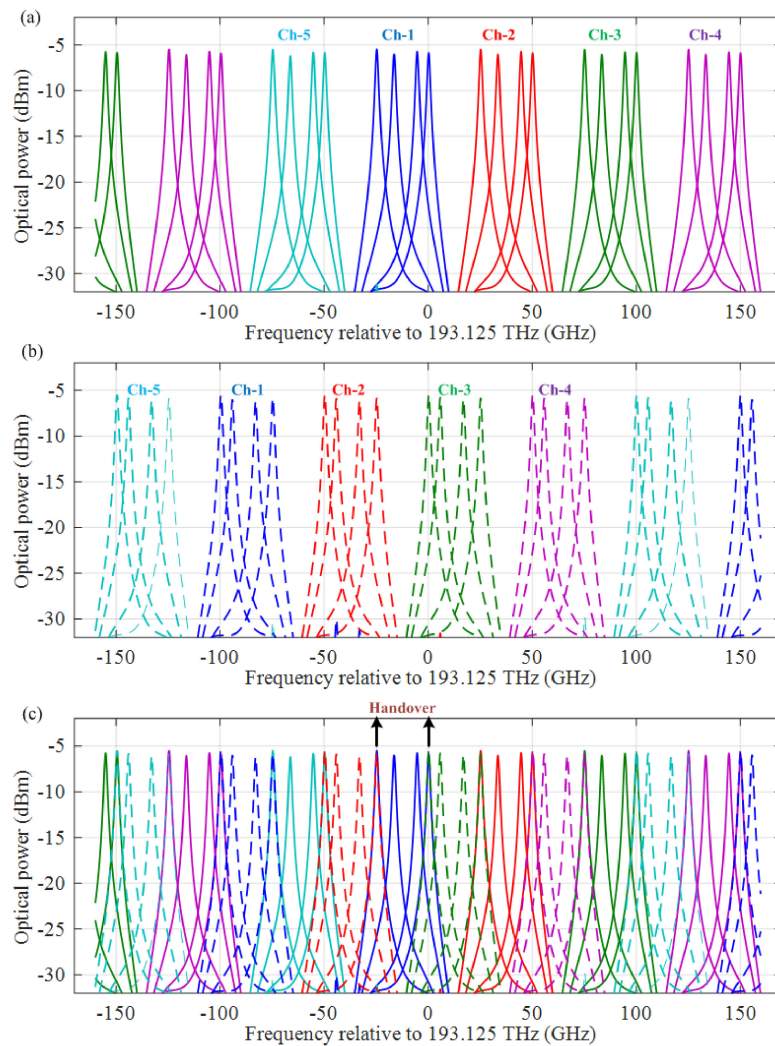
Fig. 8. A simulation of the complete spectrometer circuit with the MRR in place (as in Fig. 1) illustrating operation over complete scanning cycle over the full 50 GHz RR FSR. (a) Upper MZDI selected phase of scanning cycle; (b) lower MZDI selected phase of scanning cycle; (c) full scanning cycle.

demonstration. The LioniX Triplex technology chosen only offers MPW runs for designs using the asymmetric double strip (ADS) waveguide and the low-cost photolithography used has a minimum feature size of 1 um. Accordingly, the simulations of the components and sub-circuits that constitute the proposed spectrometer are designed using ADS as reference waveguide. The reference ADS used is shown in Fig. 9(a) where the width of the top side of the upper strip is 1.1 um and the etching results in sidewalls inclined at 82° relative to the horizontal axis. The Photon Design software tool FIMMWAVE was used to acquire the characteristics of the waveguide in the C-band. Simulations all use the TE-like mode as it is more tightly confined and hence exhibits slightly lower bend loss than the TM mode.

The effective group index of the mode is illustrated in Fig. 9(b) and has a value of 1.7725, 1.76841 and 1.7629 at the short wavelength edge (1530 nm), centre wavelength (1545 nm), and the longer wavelength (1565 nm) edge of the C-band respectively. The major contributing mechanism is waveguide dispersion; the contribution of material dispersion is negligible in comparison. The phase shift $\varphi$ contributed by a waveguide delay line of length $l$ as a function of optical frequency $\omega$
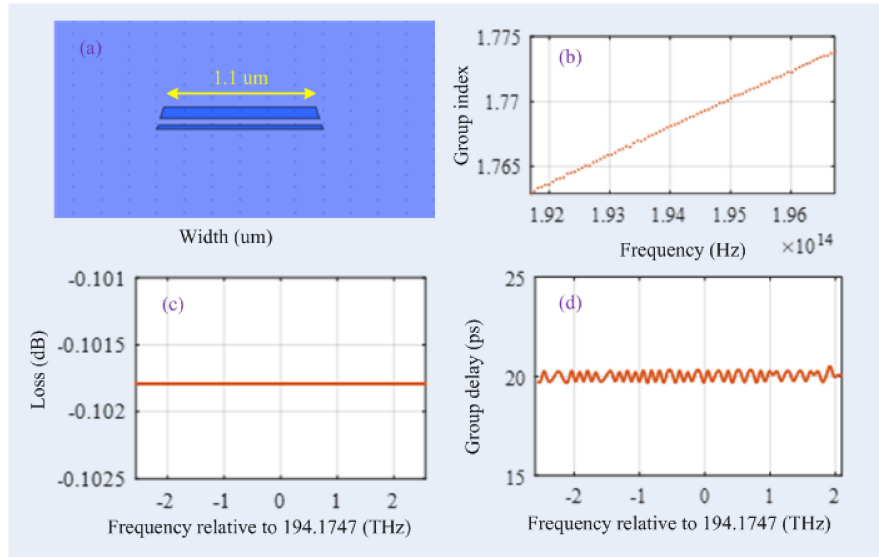
Fig. 9. (a) The reference ADS waveguide with width $w = 1.1$ $\mu m$ simulated shown in the FIMMPROP device window; (b) fundamental TE-like mode group index versus vacuum wavelength across the C-band; (c) simulated waveguide loss for a straight waveguide having length of $l = 3392.878$ $\mu m$; (d) simulated group delay caused by the same waveguide mentioned in (c).

is given by:

$$\varphi\ (\omega) = n_e\ (\omega)\ (l/c)\ \omega \tag{6}$$

where $n_e$ is the mode effective index and $c$ is the vacuum velocity of light. At frequencies in a neighborhood of a reference frequency $\omega_0$ the frequency dependence of the optical path length is well approximated its Taylor series up to second order:

$$\varphi\ (\omega) \approx \varphi_0 - \tau\ (\omega - \omega_0) - \tau'\frac{1}{2}(\omega - \omega_0)^2 \ldots \tag{7}$$

where:

$$\varphi_0 = n_e\ (\omega_0)\ (l/c)\ \omega_0$$
$$\tau = n_g\ (\omega_0)\ (l/c)$$
$$\tau' = n_g'\ (\omega_0)\ (l/c) \tag{8}$$

and $n_g$, $n_g'$ are the mode group index and mode group index dispersion respectively. The phase bias $\varphi_0$ is equal to the phase shift evaluated at the reference frequency, $\tau$ is the group delay evaluated at the reference frequency and $\tau'$ is the group delay dispersion given by the slope of the group delay versus optical frequency.

The phase bias is sensitive to subwavelength errors in the optical path length $n_e(\omega_0)l$. A means of trimming or tuning the phase bias may therefore be necessary to correctly set the operating point of interferometric components. The free-spectral range is the frequency interval over which the phase shift changes by $2\pi$ and assuming small dispersion is given by:

$$FSR\ (\omega) = c/n_g\ (\omega)\ l \tag{9}$$

The dispersion results in a small change over the band of the local value of the FSR. The FSR at the reference frequency defines a regular frequency grid over the whole band. The optical path length $l$ is calculated as 3392.878 um at the reference frequency 194.1747 THz (wavelength of 1545.0 nm). Fig. 9(c) shows the simulated total waveguide loss for the optical path length $l$. A loss
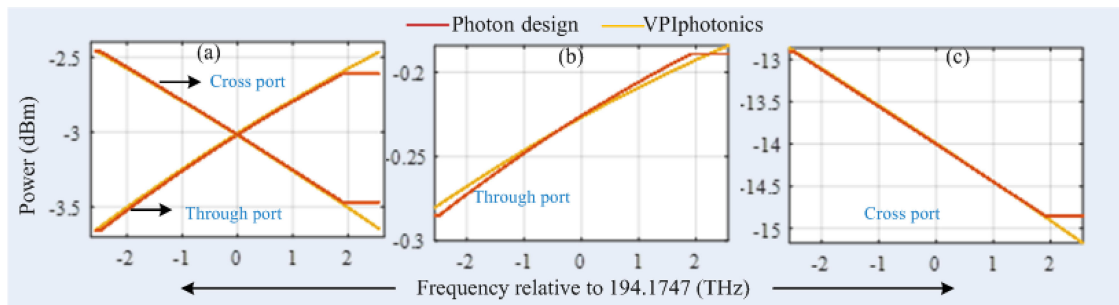
Fig. 10. (a) Power splitting of a nominally 3 dB directional coupler over the C-band for ADS waveguides and TE polarisation; (b-c) power splitting of a directional coupler used in the RR over the C-band. An input power of 0 dBm for all the samples over the C-band is used for the simulation.

of 0.3 dBcm$^{-1}$ is considered in the simulation as conservative assumption albeit $0.1 - 0.2$ dBcm$^{-1}$ is reported in the chosen platform. In the presence of dispersion, the frequencies where the phase shift returns to the value of the phase-bias position are offset from the grid because of the dispersion. Figure 9(d) shows the simulated group delay for the whole C-band. It shows that the group delay offset by $\pm0.3$ ps from its average value 20 $ps$ (50 GHz) due to waveguide dispersion. As such the FSR differ around 100 MHz from its design value, i.e 50 GHz.

The spectrometer circuit shown in Fig. 1 contains a total of three MZI sub-circuits (an MZI switch that selects one of two MZDI AWG passband flattening sub-circuits) formed by a total of six $2 \times 2$ 3 dB couplers. A $2 \times 2$ multimode interference coupler (MMI) can also be an ideal candidate for the 3 dB couplers. However, LioniX advised, for their integration platform, the excess insertion loss of MMI is much higher than directional couplers (DC). Simulations confirm that, with careful design for this platform, the excess loss of a DC is negligible ($< 0.1$ dB) comparison to an MMI ($<1$dB). However, the spectrometer circuit must operate successfully over the whole extent of the C-band. Deviations of the splitting ratio from 50:50 of 3 dB couplers impacts adversely on the channel leakage of the spectrometer and consequently the wavelength dependence of the splitting ratio of the 3 dB couplers is an important consideration. Fig. 10 (a) shows the power splitting ratio of the designed DC. First of all, the DC coupler is designed using Photon Design software tool for the reference ADS waveguide. Later on, a frequency dependent coupling coefficient is defined in VPI using the PYTHON language to emulate the findings using Photon Design. The flat power splitting at the right edge of the picture is just a continuation from the end of the frequency dependent splitting modelled in the PYTHON script. The frequency dependent coupling coefficient is defined till 194.1747+2 THz. It shows that both simulations match each other well. Furthermore, it is also noted that the wavelength dependence of the splitting ratio of an MZI sub-circuit formed by a pair of DC interconnected with a pair of waveguide arms may be engineered to be maximally flat by appropriate adjustment of the lengths of the DC and the path imbalance between them [16]. Fig. 10 (b-c) shows the simulated through port and cross port coupling of the directional coupler used in the ring resonator. The power splitting ratio is used as 94.92% and 3.98% at the design wavelength 1545 $nm$. For an FSR of 50 GHz at 1545 $nm$ the ADS waveguide ring circumference is calculated to be 3.3928 $mm$ corresponding to a ring radius of 539.99 $\mu m$. The bend loss of an ADS waveguide bend of this radius of curvature is negligible over the C-band; the mode is fully bound by the waveguide bend and the only terms contributing loss are absorption and scattering loss. Detailed data on absorption and scattering loss is not available beyond the disclosure that the total waveguide loss is circa $0.1 - 0.2$ dB $cm - 1$ for a ring of $50 - 100$ $\mu$m radii. As a conservative assumption, the waveguide loss is considered as 0.3 dB/$cm$ in the simulation. Fig. (11) shows the transmission of the RR. The zoom-out inset shows that the FSR is slightly offset from the 50 GHz grid at the edges of the band. Furthermore, the peak transmission is not constant throughout the C-band, it varies 1-1.25 dB from one edge of the C-band to the other edge. This peak transmission
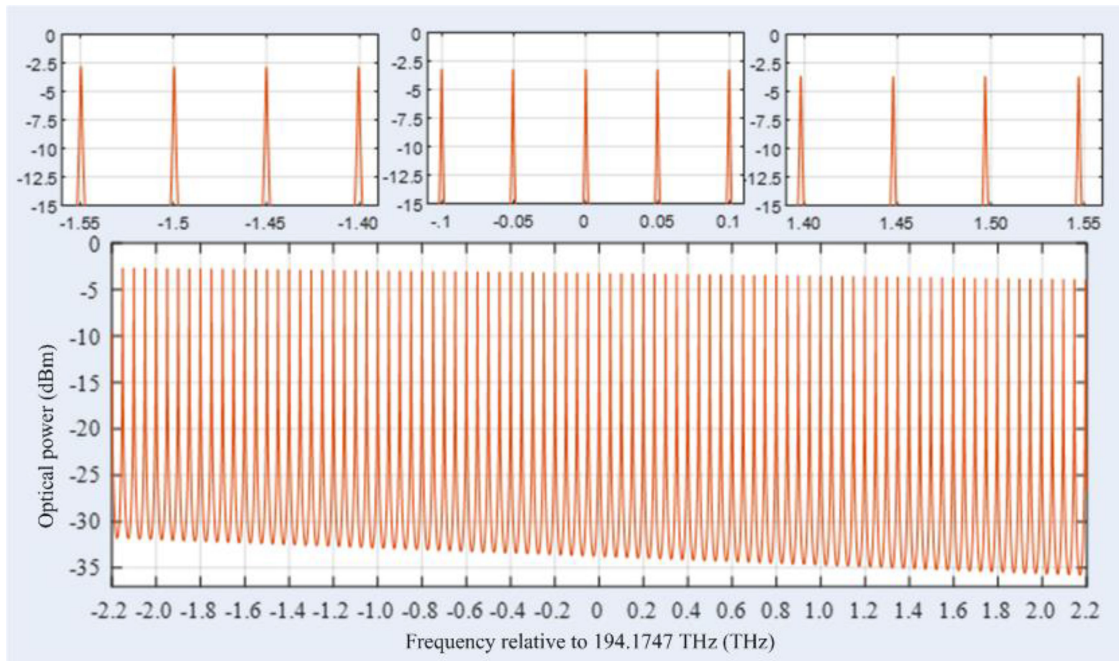
Fig. 11. The transmission of a ring resonator predicted by VPI simulation. The in set shows the zoom-in transmission at the smaller wavelength, center wavelength and longer wavelength. The coupler used has excess loss of 1.1%, cross-coupling of 3.98% and hence through-coupling of 94.92% at the design wavelength. The waveguide loss is 0.3 dB/cm. The resulting FWHM bandwidth is ($\leq$1 GHz) and insertion loss is 3.2 dB.

follows the cross-coupling characteristic curve of the DC used in the RR. The resulting resolution bandwidth is found to be around 1 GHz and the insertion loss is 3.2 dB at the design wavelength.

Ring resonators fabricated via the LioniX MPW run will be tuned by thermo-optic phase shift elements which use chromium metal films deposited on top of the cladding at a distance of roughly 8 $\mu m$ from the waveguide core as the heating element. The chromium films have 150 nm thickness and 20 $\mu m$ width and are conveniently located on the over-cladding immediately above the waveguide core section in order to ensure maximum heat transfer. The heat increases the temperature of the waveguide causing a change in effective refractive index of the mode due to the temperature dependence of the refractive indices of core and cladding materials. The change of mode effective index in turn shifts the resonant frequency of the ring.

The MPW process offers no design freedom in respect of this structure such as the use of deep trenches to prevent heat spreading. A high bit ($\geq$ 8) digital to analog converter (DAC) with moderate sampling rate ($\sim$ 256 kbit/s) will be used to precisely tune the RR over one FSR. However, electro-optic tuning offer greater efficiencies, such as low drive voltage, high extinction ratio, low drive power, linear voltage to index relationship [17]. Tuning by means of Piezo-electric actuator is found to be efficient as well [18].

A stigmatic imaging methodology has been adopted for preliminary AWG design to avoid prolonged and complex simulations when making small adjustments. For stigmatic images, the AWG channel passband characteristics are determined entirely by the transmission of an offset junction between an input (Tx) and output (Rx) waveguide respectively. Seyringer has reported impressive agreement of simulations and experimental measurements of a 160 $\times$ 50 GHz AWG fabricated in $Si_3N_4$ with footprint of $\sim$1 cm² [14]. Her biomedical sensing application dictates the operating center vacuum wavelength of 850 nm. However, a reference design for 850 $nm$ may be mapped to 1550 $nm$ by increasing all dimensions by a factor of 1.8 at least as a good starting

TABLE 4
Operation of the Switch

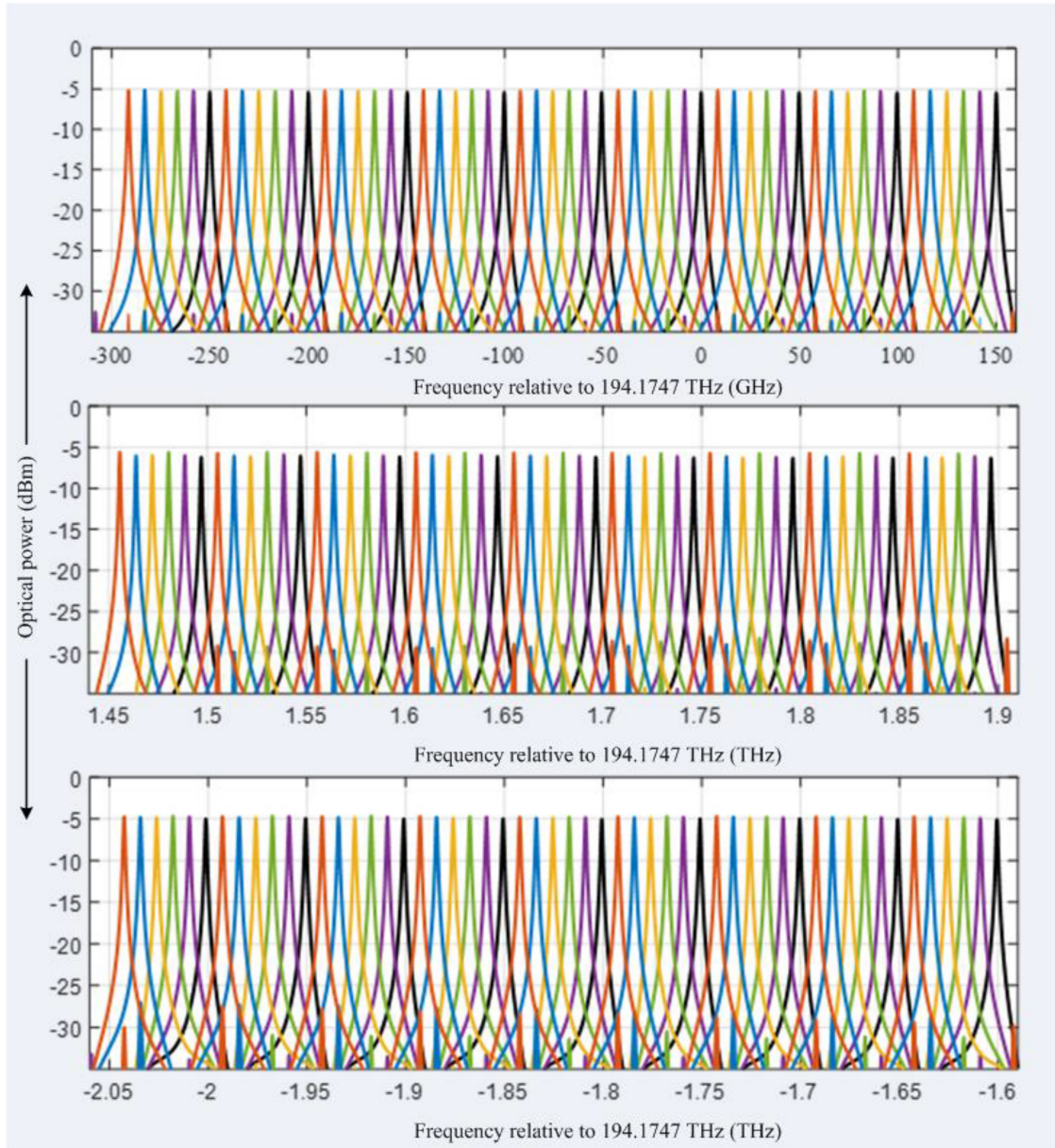| RR position | Switch position | Remarks |
|---|---|---|
| 0˚ to 180˚ | A (Fig.1 ) | Upper MZI is in operation |
| 180˚ to 360˚ | B (Fig. 1) | Lower MZI is in operation |



Fig. 12. Full scanning cycle of the spectrometer at the center of the C-band (top), lower wavelength edge (middle) and longer wavelength edge (bottom).
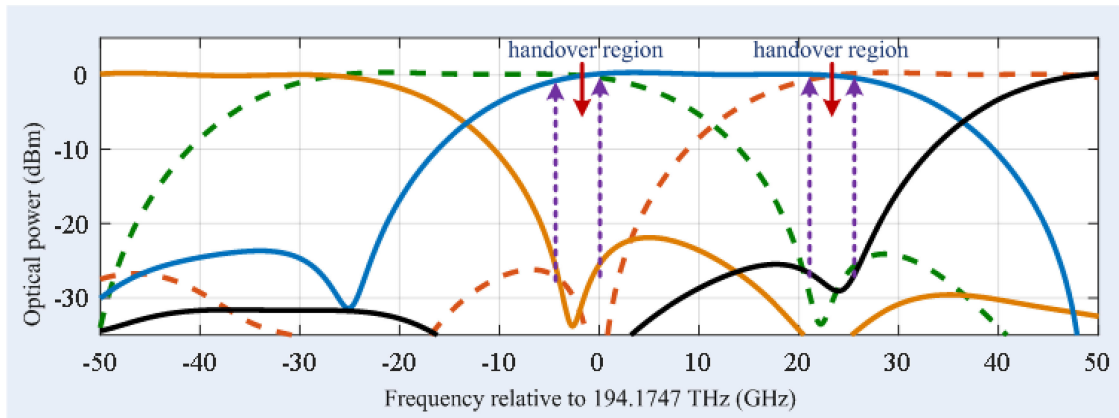
Fig. 13. Zoom-out view of MZI-AWG interlaced spectra to find out exact switching position.

point for further optimisation. Moreover, the spectrometer requires almost half the number of output channels which will scale down the footprint. Finally, VPI circuit simulation is used to evaluate the overall performance of the proposed circuit. An AWG having 80 output ports with 50 GHz FSR is used in the circuit simulation. An AWG insertion loss of 5 dB is considered representative, while a random 100 MHz offset/shift from the 50 GHz FSR is applied to emulate the fabrication error. The RR, DC and MZI is configured as depicted earlier in the discussion part. It is reasonable to assume that all directional couplers on the same integrated circuit have similar extinction ratio as Yamazaki *et al.* [19] obtained less than 0.5 dB loss variation among 4 Mach Zehnder Modulators (MZMs). An optical source covering the whole C-band with power of 0 dBm for all the samples is used as input. The spectrometer performs excellently albeit the crosstalk is increased by 2-5 dB at some points. Nevertheless, a crosstalk of $-22$ dB or less is obtained as shown in Fig. 12 . Again, the peak power flatness lies within 1 dB.

The entire operation of the proposed circuit requires four controls; two static and two dynamic. As per the 1$^{st}$ term of Eq. (8), the two MZI connected to the AWG will have phase bias at the design wavelength. Hence, phase tuning is required to align the FSR of the MZI with the channel spectra of the AWG. Once this is done, it will remain static for the whole operation. Light can be launched using the unused port of the switch to complete this adjustment. Out of the two-dynamic control, one will tune the RR over one FSR and other will trigger the switch at the predefined position. Table 4 shows the operation of the switch:

The handover of the switch is not strictly restricted to Table 4. If we look closely at the ganged MZI-AWG spectra, there is ample liberty for the switching operation. The switch does not need to toggle at the exact 180° and 360° (or 0°) position of the RR. Rather there is a window of 5 GHz to make this switching operation with negligible power penalty. This redefines switching range 180 $\pm$ 15°. An integrated wave meter as presented in [20], will be used to monitor the position of each resonance within an AWG channel. The wave meter circuit consist of a 2 $\times$ 2 directional coupler (or 2 $\times$ 2 MMI) and a 3 $\times$ 3 MMI (with its middle input port unused) that forma two-arm interferometer with a delay imbalance. When driven by a source with a narrow spectral line shape, in the present case a RR resonance within an AWG channel passband it generates sinusoidal interference fringes when the frequency is scanned. The phase of the fringe is a measure of the position of the spectral line within the FSR of the interferometer. The 3 $\times$ 3 MMI introduces 120° phase shifts between three copies of the intensity fringes measured at its three outputs, which enables an accurate estimate of the frequency of the spectral line independent of the input intensity and robust to component impairments.

## 5. Conclusion

In summary, a state of the art on-chip spectrometer with sub-GHz resolution over the entire C-band in a compact footprint has been proposed and verified by simulation in this article. To the best of the authors knowledge there have been no reports of simulation or experimental studies of a sub-GHz integrated spectrometer operating over the entire C-band and the solution proposed herein is unique. The proposed circuit architecture is feasible for photonic integration in the CMOS compatible $Si_3N_4$ platform owing to its low loss mature technology.

## Acknowledgment

## References

[1] S. Gringeri, N. Bitar, and T. J. Xia, "Extending software defined network principles to include optical transport," *IEEE Commun. Mag.*, vol. 51, no. 3, pp. 32–40, Mar. 2013.

[2] A. Aguado *et al.*, "Dynamic virtual network reconfiguration over SDN orchestrated multitechnology optical transport domains," *J. Lightw. Techn.*, vol. 34, no. 8, pp. 1933–1938, Apr. 2016.

[3] O. G. Dios *et al.*, "First demonstration of multi-vendor and multi-domain EON with S-BVT and control interoperability over pan-European testbed," in *Proc. Eur. Conf. Opt. Commun.*, Valencia, Spain, Sep. 2015, pp. 1–3.

[4] F. Meng *et al.*, "Robust self-learning physical layer abstraction utilizing optical performance monitoring and Markov chain Monte Carlo," in *Proc. Eur. Conf. Opt. Commun.*, Gothenburg, Sweden, Sep. 2017, pp. 1–3.

[5] B. Kyotoku, L. Chen, and M. Lipson, "Sub-nm resolution cavity enhanced micro-spectrometer," *Opt. Express,* vol. 18, no. 1, pp. 102–107, Jan. 2010.

[6] G. Yurtsever, and R. Baets, "Integrated spectrometer on silicon on insulator," in *Proc. 16th Annu. Symp. IEEE Photon.*, Ghent, Belgium, 2011, pp. 273–276.

[7] E. Ryckeboer *et al.*, "Silicon-on-insulator spectrometers with integrated GaInAsSb photodiodes for wide-band spectroscopy from 1510 to 2300 nm," *Opt. Express*, vol. 21, no. 5, pp. 6101–6108, Mar. 2013.

[8] C. Xiang, P. A. Morton, J. Khurgin, C. Morton, and J. E. Bowers, "Widely tunable Si3N4 triple-ring and quad-ring resonator laser reflectors and filters," in *Proc. IEEE 15th Int. Conf. group IV Photon.*, Cancun, Mexico, Aug. 2018, pp. 1–2.

[9] Y. Li *et al.*, "On-chip photonic microsystem for optical signal processing based on silicon and silicon nitride platforms," *Adv. Opt. Technologies*, vol. 7, no. 1-2, pp. 81–101, Apr. 2018.

[10] M. Kita *et al.*, "On-chip infrared spectroscopic sensing: Redefining the benefits of scaling," *IEEE J. Sel. Topics Quantum Electron.*, vol. 23, no. 2, pp. 340–349, Sep. 2017.

[11] C. G. H. Roeloffzen *et al.*, "Low-loss Si3N4TriPleX optical waveguides: Technology and applications overview," *IEEE J. Sel. Topics Quantum Electron.*, vol. 24, no. 4, pp. 1–21, Jan. 2018.

[12] L. Zhuang, D. Marpaung, M. Burla, W. Beeker, A. Leinse, and C. Roeloffzen, "Low-loss, high-index-contrast Si3N4/SiO2 optical waveguides for optical delay lines in microwave photonics signal processing," *Opt. Express*, vol. 19, no. 23, pp. 23162–23170, Nov. 2011.

[13] Y. Xie, L. Zhuang, and A. Lowery, "Picosecond optical pulse processing using a terahertz-bandwidth reconfigurable photonic integrated circuit," *Nanophotonics*, vol. 7, no. 5, pp. 837–852, May 2018.

[14] D. Seyringer *et al.*, "Technological verification of size-optimized 160-channel silicon nitride-based AWG-spectrometer for medical applications," *Appl. Phys. B*, vol. 125, no. 6, p. 88, Jun. 2019.

[15] T. Hall, M. Hasan, M. Rad, and D. Patrick, "Optical performance monitor," U.S. patent application 62/868,450, Jun. 2019.

[16] B. E. Little and T. Murphy, 'Design rules for maximally flat wavelength-insensitive optical power dividers using Mach–Zehnder structures', *IEEE Photon. Technol. Lett.*, vol. 9, no. 12, 1607–1609, 1997.

[17] A. Naim *et al.*, "Tunable hybrid silicon nitride and thin-film lithium niobate electro-optic microresonator," *Opt. Lett.*, vol. 44, no. 3, 618–621, 2019.

[18] W. Jin, R. G. Polcawich, P. A. Morton, and J. E. Bowers, "Piezoelectrically tuned silicon nitride ring resonator," *Opt. Express*, vol. 26, no. 3, 3174–3187, 2018.

[19] H. Yamazaki, T. Saida, T. Goh, S. Mino, M. Nagatani, H. Nosaka, and K. Murata, "Dual-carrier dual-polarization IQ modulator using a complementary frequency shifter," *IEEE J. Sel. Topics Quantum Electron.*, vol. 19, no. 6, pp. 172–182, May 2013.

[20] E. Kleijn, E. M. van Vliet, D. Pustakhod, M. K. Smit, and X. J. M. Leijtens, "Amplitude and phase error correction algorithm for 3X3 MMI based Mach–Zehnder interferometers," *J. Lightw. Technol.*, vol. 33, no. 11, pp. 2233–2239, Jun. 2015.